Supporting Information

Carbon Black Supported FM-N-C (FM=Fe, Co, Ni) Single-Atom Catalysts Synthesized by Self-Catalysis of Oxygen Coordinated Ferrous Metal Atoms

Lina Wang,[‡ a] *Junwei Zhang,*[‡ b,c] *Lirong Zheng,*[d] *Jiarui Yang,*[a] *Yongcheng Li,*[a] *XinWan,*[a] *Xiaofang Liu,*[a] *Xixiang Zhang,*[c] *Ronghai Yu*[a] *and Jianglan Shui* [*, a]

[a] School of Materials science and engineering, Beihang University,
No. 37 Xueyuan Road, Beijing 100083, China.

[b] Key Laboratory for Magnetism and Magnetic Materials of the Ministry of Education, Lanzhou University,
No. 222 Tianshui Road, Lanzhou 730000, China.

[c] Physical Science and Engineering Division (PSE), King Abdullah University of Science and Technology (KAUST),
Thuwal 23955–6900, Saudi Arabia.

[d] Beijing Synchrotron Radiation Facility, Institute of High Energy Physics, Chinese Academy of Sciences,
No. 19 Yuquan Road, Beijing 100049, China.

*Corresponding author E-mail address: shuijianglan@buaa.edu.cn

[‡] These authors contributed equally to the work.

Experimental

Chemicals

Black Pearls 2000 (BP) was purchased from Cabot Corporation. Sulfuric acid (98%), nitric acid (70%), ethanol, potassium thiocyanate and potassium hydroxide were obtained from Beijing Chemical Works. Perchloric acid (70%) was obtained from Sinopharm Chemical Reagent Co., Ltd. Ferrous acetate ($Fe(Ac)_2$) was purchased from Aladdin Industrial Corporation. Cobalt (Ⅱ) acetate terahydrate ($Co(Ac)_2 \cdot 4H_2O$) and nickel (Ⅱ) acetate terahydrate ($Ni(Ac)_2 \cdot 4H_2O$) were purchased from Guangdong Chemical Reagent Engineering-technological Research and Development Centre. Ultrapure water with the specific resistance of 18.23 MΩ cm was obtained by reversed osmosis followed by ion exchange and filtration. 20 wt% Pt/C catalyst was purchased from Johnson Matthey. Potassium bicarbonate was purchased from Shanghai Macklin biochemical Co., Ltd. All reagents were of analytical grade and used as received without further purification.

Catalyst preparation

500 mg Black Pearls 2000 (BP) were refluxed in a 80 ml 1:1 v/v solution of sulfuric acid (98%) and nitric acid (70%) at 60 ℃ for 1 h and continuously stirred at 10 ℃ for 40 h to introduce surface oxygenic functional groups. The treated BP was repeatedly washed with water during vacuum filtration and dried at 60 ℃ in vacuum. Subsequently, 100 mg preoxidized BP was dispersed in 50 ml ethanol solution containing 0.02 mmol bivalent metal acetate ($Fe(Ac)_2$, $Co(Ac)_2 \cdot 4H_2O$, or $Ni(Ac)_2 \cdot 4H_2O$) by sonifier cell disrupter for 10 min, and then stirred for 24 h to allow for adequate absorption of the bivalent metal ions (Fe^{2+}, Co^{2+} and Ni^{2+}). The mixture was collected by vacuum filtration and dried at 60 ℃ in vacuum, and followed by a heating at 600 ℃ for 3h under NH_3 flow.

Materials characterization

The morphology and microstructure of samples were investigated by field-emission scanning electron microscopy (FESEM, JSM-7500, JEOL, Japan) and high

resolution transmission electron microscopy (HRTEM, JEM 2100F, 200 kV). X-ray diffraction (XRD) patterns were obtained using an X-ray diffractometer (Rigaku D/Max 2500) equipped with a Cu Kα irradiation. Atomic resolution structures of the samples were observed using a high-angle annular dark-field scanning transmission electron microscopy (HAADF-STEM, Titan Cubed Themis G2 300) operated at 200 kV. The X-ray photoelectron spectroscopy (XPS) analysis was performed on ESCALAB 250Xi using monochromatic Al Kα radiation. Inductively coupled plasma optical emission spectrometry (ICP-OES) was carried out on Optima-7000DV. N_2 sorption isotherms were measured by the AS-6B system (Quantachrome Instruments) at 77.3 K and the porosity parameters were calculated using the software QuadraWin (version 6.0). The specific surface area was obtained using the Brunauer–Emmett–Teller（BET）method. The pore size distribution was determined using quenched solid density functional theory model. The external surface area is defined as nonmicropore area, which was obtained by subtracting the micropore surface area (calculated through t-plot method) from the Brunauer–Emmett–Teller surface area. Fourier transform infrared spectroscopy (FTIR) was performed on a Nicolet IS10 FTIR spectrophotometer on KBr pellets. Laser Confocal Raman Microspectroscopy were measured by the Renishaw inVia. X-ray absorption spectroscopy (XAS) was performed at room temperature on the 1W1B beamline at BSRF (Beijing Synchrotron Radiation Facility). Fluorescence-mode Fe (Co and Ni) K-edge XAFS data of Fe-N/BP (Co-N/BP and Ni-N/BP) and Fe-O/BP (Co-O/BP and Ni-O/BP) were collected, where a 100% Ar filled Lytle ion-chamber detector with Mn (Fe and Co) X-ray filters and soller slits were used. The absorption spectra of reference Fe_2O_3 (Co_3O_4 and NiO), FePc (CoPc and NiPc) were collected in transmission mode. The monochromator energy was calibrated using a Fe (Co and Ni) foil. The XAFS data were analyzed using IFEFFIT.

Electrochemical Testing

ECSA was estimated from the electrochemical double-layer capacitance of the catalytic surface. To measure double-layer charging via CV, a potential range in which no apparent Faradaic processes occur was determined from static CV. Here, the

potential range of 0.92-0.94 V was selected. All measured current in this non-Faradaic potential region is assumed to be due to double-layer charging. The ECSA can be estimated using the equation:

$$ECSA = \frac{i}{v * m * C_{gc}}$$

where i is the current, m is the electrode mass, v is the scan rate and C_{gc} is the double layer capacitance (F m^{-2}) of the glassy carbon electrode surface, for which the typical value of 0.2 F m^{-2} was used.

ORR Electrochemical experiments were performed with a bipotentiostat (CHI 760E, CH Instruments) and rotator (AFMSRCE, Pine Research Instrumentation) at 25 ℃ using a three-electrode electrochemical cell. Saturated calomel electrode (SCE) and Hg/HgO electrode were respectively used for reference electrodes in acidic and alkaline electrolytes, and graphite rod was used as the counter electrode. The acidic and alkaline electrolytes were 0.5 M H_2SO_4 (or 0.1 M $HClO_4$ for Pt/C) and 0.1 M KOH, respectively. The potentials obtained in 0.5 M H_2SO_4, 0.1 M $HClO_4$ and 0.1 M KOH were converted to the reversible hydrogen electrode (RHE) scale by a shift value of 0.273 V, 0.303 V and 0.865 V, respectively. A rotating ring-disk electrode (RRDE, 5.61 mm of disk outer diameter, Pine Research Instrumentation) was used as the working electrode. Prior to every measurement, the RRDE was polished with 300 nm alumina powders and then with 50 nm alumina powders to afford a mirror finish. To prepare the catalyst ink, 1.5 mg of the catalyst or 1 mg Pt/C catalyst was mixed with 43.00 uL deionized water, 54.75 uL isopropanol, and 2.15 uL Nafion® alcohol solution (5 wt%, Aldrich), and the resulting slurry was ultrasonicated for 15 min. The 10 μL catalyst ink was pipetted with a micropipette onto the glassy carbon disk and dried in the air, resulting in a catalyst loading of ca. 600 μg cm^{-2}. A Pt/C (20 wt%) catalyst with a loading of 40 μg $_{Pt}$ cm^{-2} was used as a reference. Before ORR electrochemical tests, the electrolyte was saturated with Ar or O_2 and the gas flow was maintained during the experiments. The resultant current was obtained by subtracting the background current measured in the Ar-saturated electrolyte from the original linear sweep voltammetry (LSV) measured in the O_2-saturated electrolyte. LSV was conducted between 0.2 and 1.2 V vs. RHE for

ORR at 1600 rpm with a sweep rate of 10 mV s^{-1}. The ring voltage for RRDE measurement is set at 1.25 V *vs* RHE. The peroxide yields were calculated from the ring current (I_r) and the disk current (I_d) by using the equation:

$$H_2O_2(\%) = 200 \times \frac{I_r}{I_r + 0.37 I_d}$$

The electron transfer number in acid was computed by the equation:

$$n = \frac{4I_d}{I_d + \frac{I_r}{0.37}}$$

where

I_r : ring current

I_d : disk current

The collection efficiency was 37%.

The CO_2 reduction experiments were performed in a gastight H-type glass cell with two-compartments separated by Nafion 211 membrane (DuPont). Each compartment contained 25 ml 0.5 M $KHCO_3$ electrolyte with approximately 25 ml headspace. A flow of CO_2 (20 sccm, 99.99%), monitored by a mass flow controller (S500, Horiba Metron), was purged into the cathodic compartment during the measurement to remove residual air and ensure continuous CO_2 saturation in a three-electrode system at an electrochemical workstation. The Pt wire and Ag/AgCl electrodes (with saturated KCl solution) served as the counter electrode and the reference electrodes, respectively. In a typical synthesis of the working electrode, a catalyst ink was prepared by dispersing 1 mg of catalyst into 950 uL ethanol and 50 μL Nafion solution (5 wt%, Aldrich) with 10 min sonication. The catalyst ink (200 uL) was loaded and dried into the 1×1 cm^2 carbon paper. For the stability test, 500 uL of the ink was loaded onto a carbon fiber paper toward a mass loading of 0.5 mg cm^{-2}. All potentials measured against a saturated Ag/AgCl electrode were converted to the RHE scale in this work using E (vs. RHE) = E (vs. Ag/AgCl) + 0.1989 V + 0.0591 × pH, where pH values of electrolytes were determined by a pH Meter (PHS-3C, Shanghai Yueping Instrument). The gas products were sampled and detected by gas chromatograph (GC-2030, Shimadzu) after a

continuous electrolysis of 20 min under each potential. The liquid product was characterized by 1H NMR on Bruker AVANCE III 600.

The current for gas production is calculated at a given potential as follows:

$$I_{product} = \frac{N \times F \times V \times v_{product} \times (1 \times 10^{-6}\, m^3\, ml^{-1}) \times P}{R \times T \times (60\, s\, min^{-1})}$$

$I_{product}$: partial current for certain product, A.

N: the number of electron transferred for product formation, which is 2 for CO and H_2.

F: Faradaric constant, 96485 C mol^{-1}.

V: gas flow rate measured by a flow meter at the exit of the cell at room temperature and under ambient pressure, ml min^{-1}.

$v_{product}$: volume concentration of product in the exhaust gas from the cell (GC data), vol %.

P: ambient pressure, 1.013×10^5 Pa.

R: molar gas constant, 8.314 J mol^{-1} K^{-1}.

T: room temperature, 298.15 K.

The Faradaric efficiency for gas production is calculated at a given potential as follows:

$$FE = \frac{I_{product}}{I_{total}} \times 100\ \%$$

FE: Faradaric efficiency for production.

I_{total}: steady-state cell current, A.

The TOF value for gas product was calculated as follows:

$$TOF = \frac{I_{product}/NF}{m_{cat} \times w/M} \times 3600$$

TOF: turnover frequency, h^{-1}.

m_{cat}: catalyst mass in the electrode, g.

w: metal loading in the catalyst.

M: atomic mass of metal, g mol^{-1}.

MEA Preparation and PEM Fuel Cell Tests

The catalyst Fe-N/BP and Nafion ionomer (weight ratio of 1/1) were mixed in isopropanol/water (volume ratio of 1/1) to form a uniform catalyst ink by sonication and stirring. Afterwards, the homogeneous ink was brushed onto a piece of 5 cm^2 carbon paper (gas diffusion layer, GDL) and dried at 80 °C for 2 h under vacuum. The cathode catalyst loading was 3 mg cm^{-2} for Fe-N/BP. Anode was Pt/C(20%) with a catalyst loading of 0.5 mg_{Pt} cm^{-2}. A couple of anode and cathode were hot-pressed onto a piece of Nafion 211 membrane (DuPont®) at 130 °C for 2 min under 300 pounds cm^{-2} pressure to obtain the MEA. Finally, PEM fuel cell test was performed on a fuel cell test station (Scribner 850e) with UHP grade H_2 and O_2. The gas and cell temperatures were 80 °C. The flow rate of 100% humidified H_2 and O_2 was 300 and 400 mL min^{-1}, respectively.

Computational methods

The density functional theory (DFT) calculation was performed within a generalized gradient approximation (GGA) designed by Perdew-Burke-Ernzerhof (PBE), as implemented in the Vienna ab initio simulation package (VASP). The projector augmented wave (PAW) method is used to describe the ionic potentials. The cutoff energy for the plane-wave expansion was set to 400 eV. The K-point sampling of the Brillouin zone was obtained using a 2×2×1 grid generating meshes with their origin centered at the gamma (Γ) point. All calculations were spin polarized and the force convergence criterion for atomic relaxation was 0.01 eV/Å in the optimization of structure. The likely transition state (TS) structures produced by the NEB method were further refined until the forces on the atoms were less than 0.05 eV/Å. The unit box was built with a volume of 12 Å × 12 Å × 20 Å for all calculations. All the atoms in slab

structure including adsorbates were allowed to relax in three dimensions during the optimization.

The adsorption energies $E_{ads}$for NH_3 adsorption on the surface of the catalyst precursors was calculated according to the formula:

$$E_{abs} = E_{NH_3-substrate} - (E_{NH_3} + E_{substrate})$$

where E_{NH_3}, $E_{substrate}$ and $E_{NH_3-substrate}$ represent the energy of free NH_3 molecule, the surface of catalyst precursors and NH_3 adsorbed on the surface of catalyst precursors, respectively.

The stability of various FM-O/BP and FM-N/BP models is evaluated by calculating their formation energies (E_f) according to the formula:

$$E_f = E_D - (E_P - \Delta n_C \mu_C) - \Delta n_{O/N} \mu_{O/N} - \Delta n_{FM} \mu_{FM}$$

where E_D and E_P are the energies of doped and pristine graphene sheets, respectively, u_i is the chemical potential of atomic species *i* (*i* = C, O/N, and FM), and Δn_i is the difference of atomic species i in doped and pristine graphene. Here μ_C, $\mu_{O/N}$, and μ_{FM} are referred to the energy of the C atom in graphene, half of the energy of an O_2/N_2 molecule, and the energy of the FM atom, respectively.

Supplementary Figures and Tables

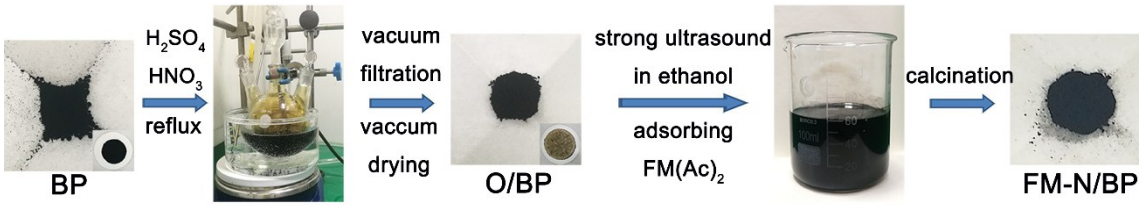

Figure S1. Synthetic procedure of FM-N/BP SACs.

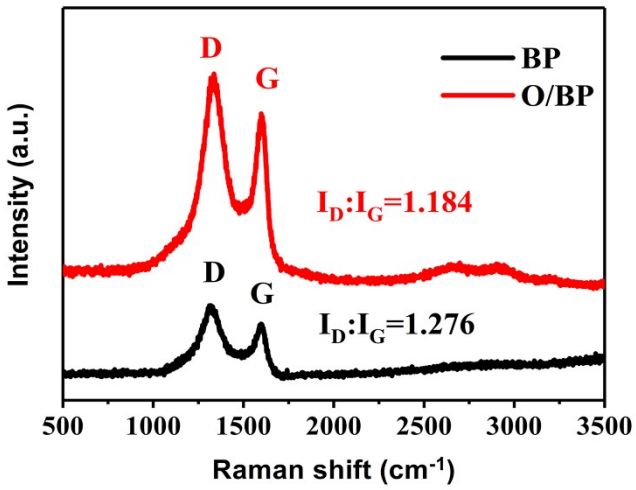

Figure S2. Raman spectra of BP and O/BP.

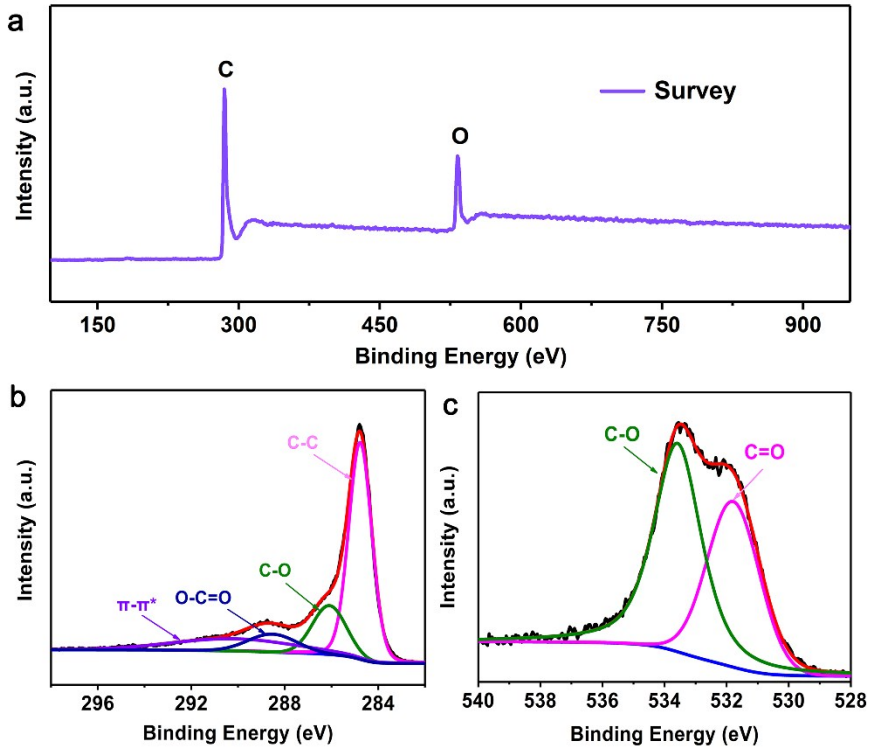

Figure S3. XPS spectra of O/BP. a) survey, b) C1s, and c) O1s spectra.

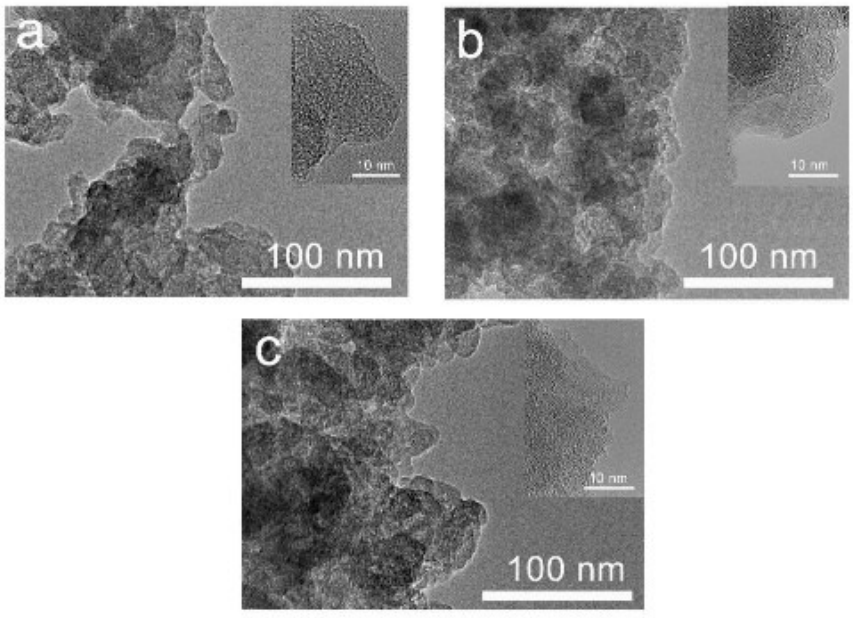

Figure S4. TEM images of a) Fe-O/BP, b) Co-O/BP and c) Ni-O/BP (Insets: high-resolution images).

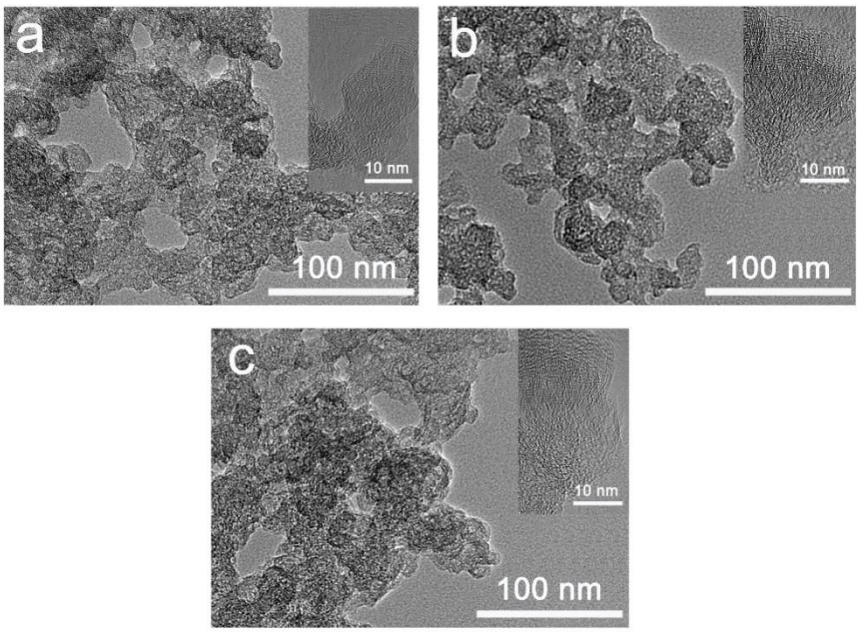

Figure S5. TEM images of a) Fe-O/BP, b) Co-O/BP and c) Ni-O/BP thermally heated at 300 ℃ under NH_3 atmosphere (Insets: high-resolution images).

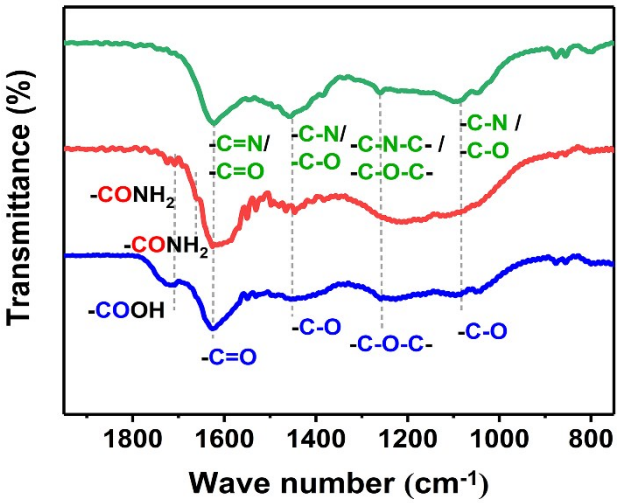

Figure S6. FTIR spectra of the Fe-O/BP (blue line), the heat-treated samples at 300 ℃ in NH_3 (red line) and the final catalyst Fe-N/BP (green line).

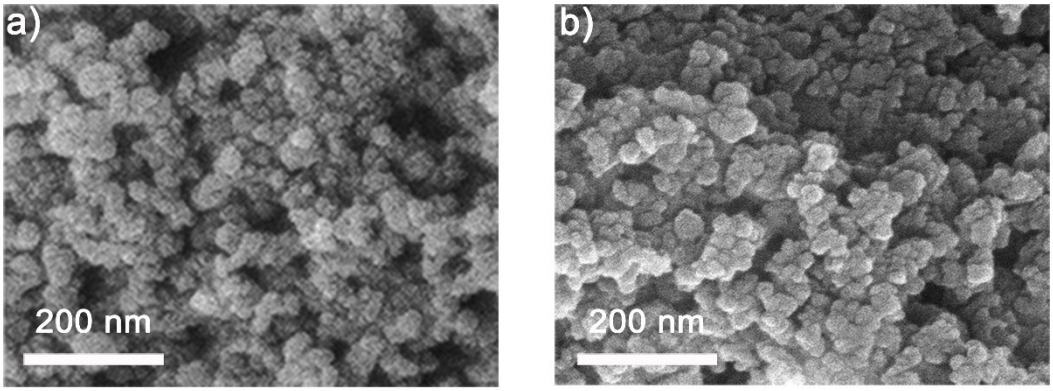

Figure S7. SEM images of BP and Fe-N/BP.

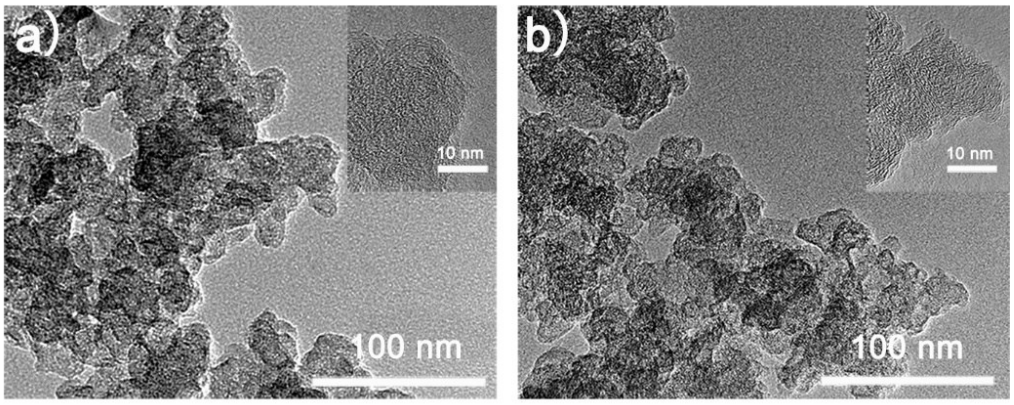

Figure S8. TEM images of a) Co-N/BP and b) Ni-N/BP (Insets: HR-TEM images).

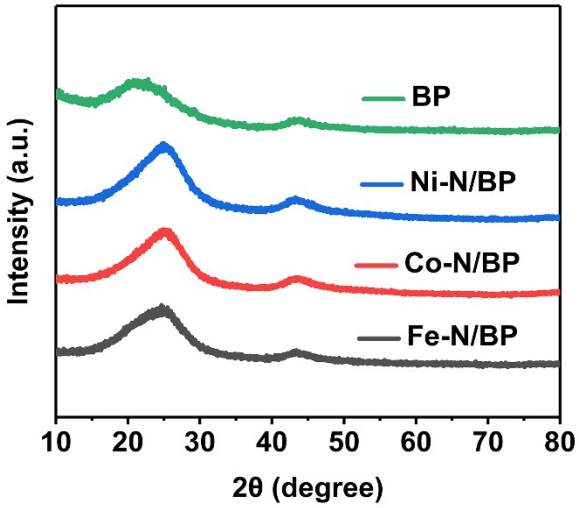

Figure S9. XRD patterns of Fe-N/BP, Co-N/BP, Ni-N/BP and BP.

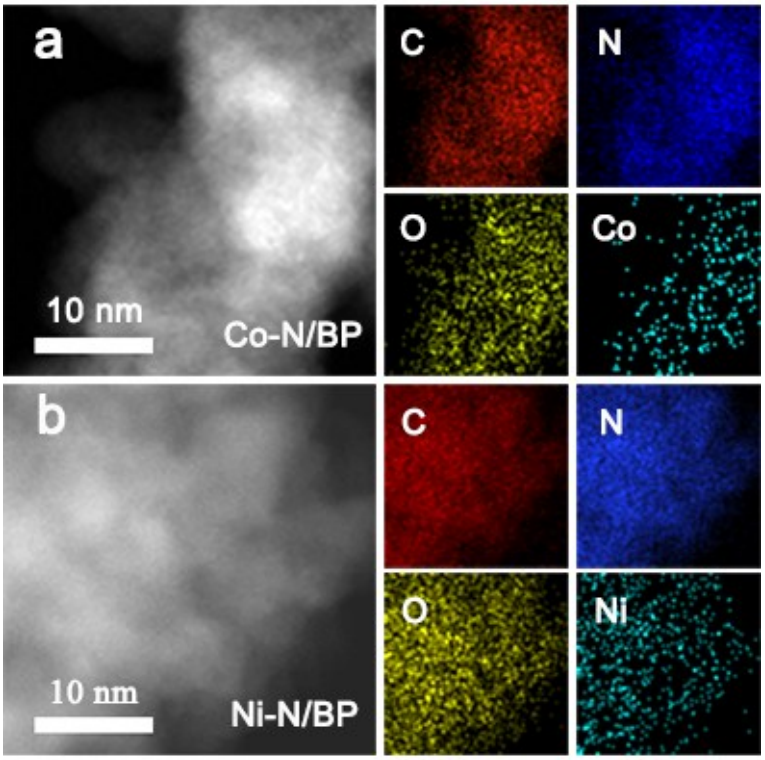

Figure S10. STEM images and corresponding elemental mappings of a) Co-N/BP and b) Ni-N/BP.

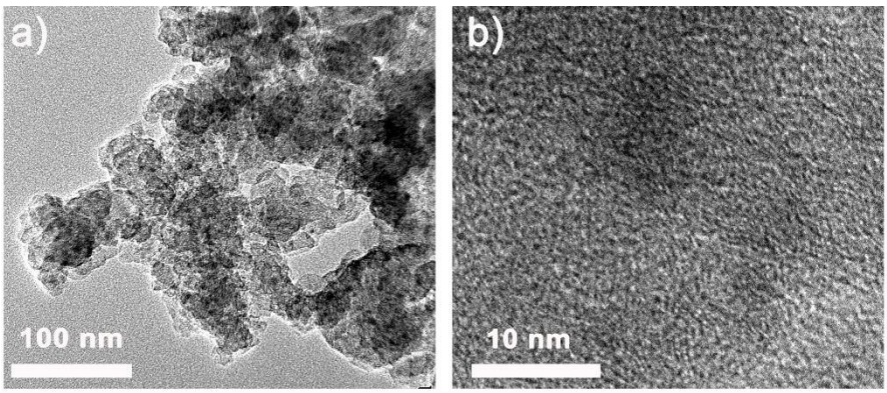

Figure S11. a) TEM and b) HR-TEM images of Fe-N/BP heated at 700 ℃, showing metal nanoparticles.

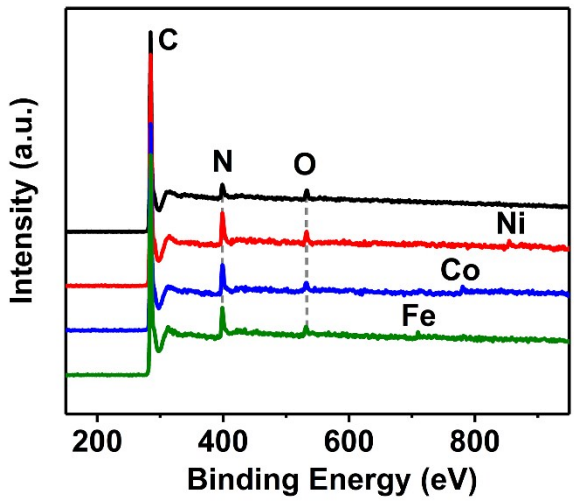

Figure S12. XPS surveys of Fe-N/BP (green line), Co-N/BP (blue line), Ni-N/BP (red line) and N/BP (black line).

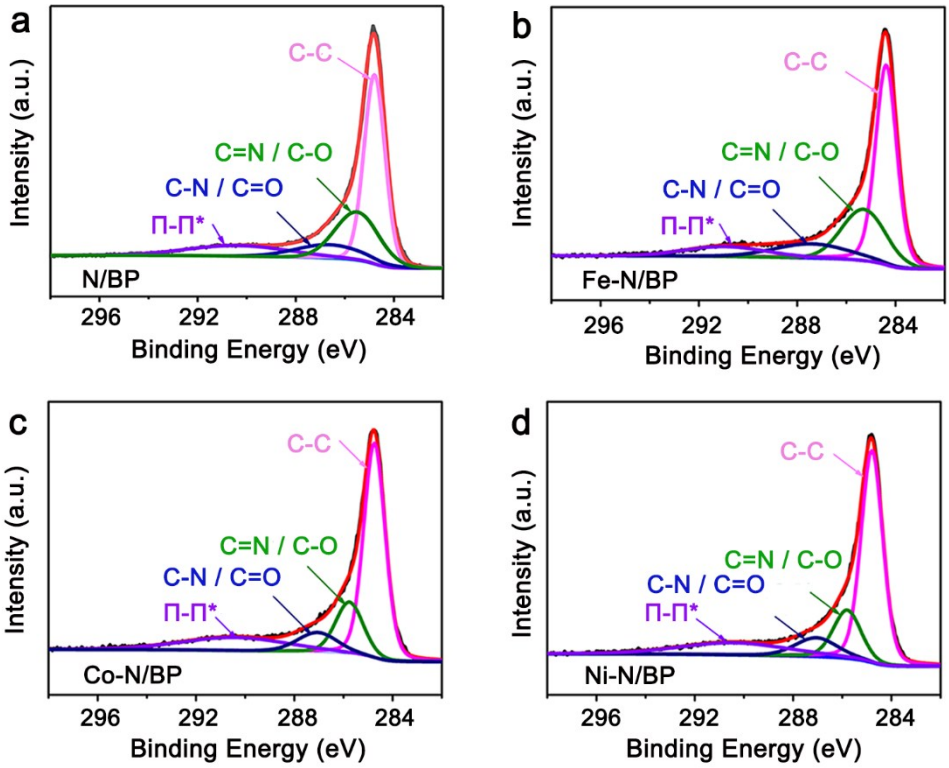

Figure S13. XPS C 1s spectra of a) N-BP, b) Fe-N/BP, c) Co-N/BP and d) Ni-N/BP.

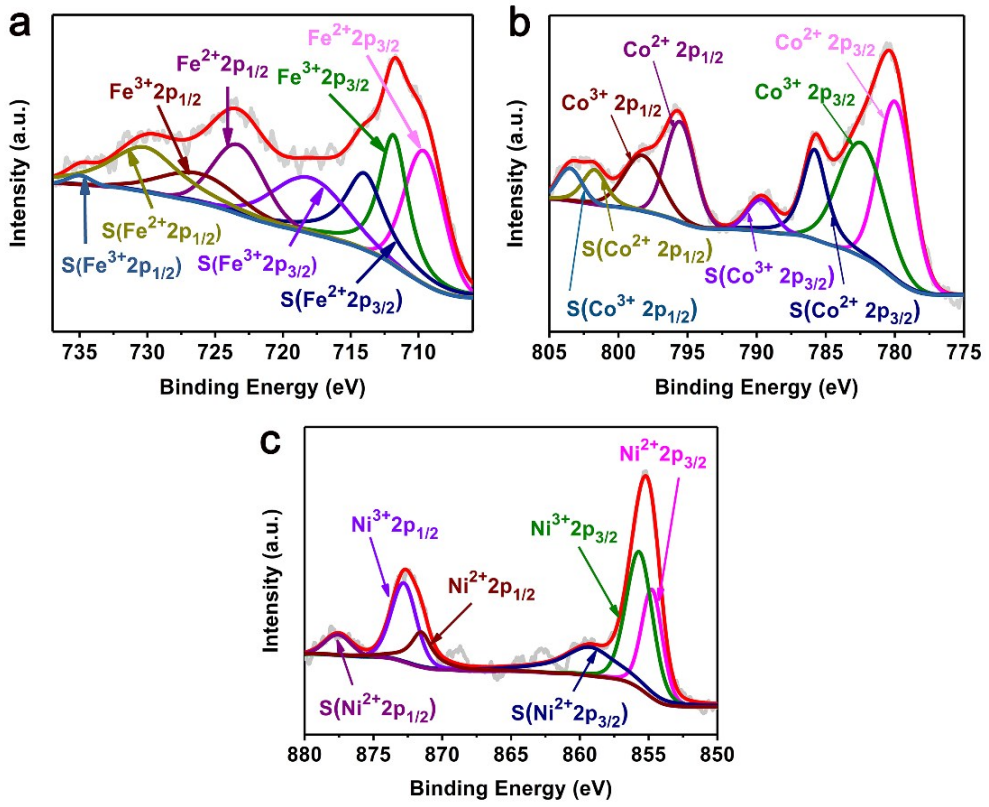

Figure S14. XPS spectra of a) Fe 2p of Fe-N/BP, b) Co 2p of Co-N/BP and c) Ni 2p of Ni-N/BP.

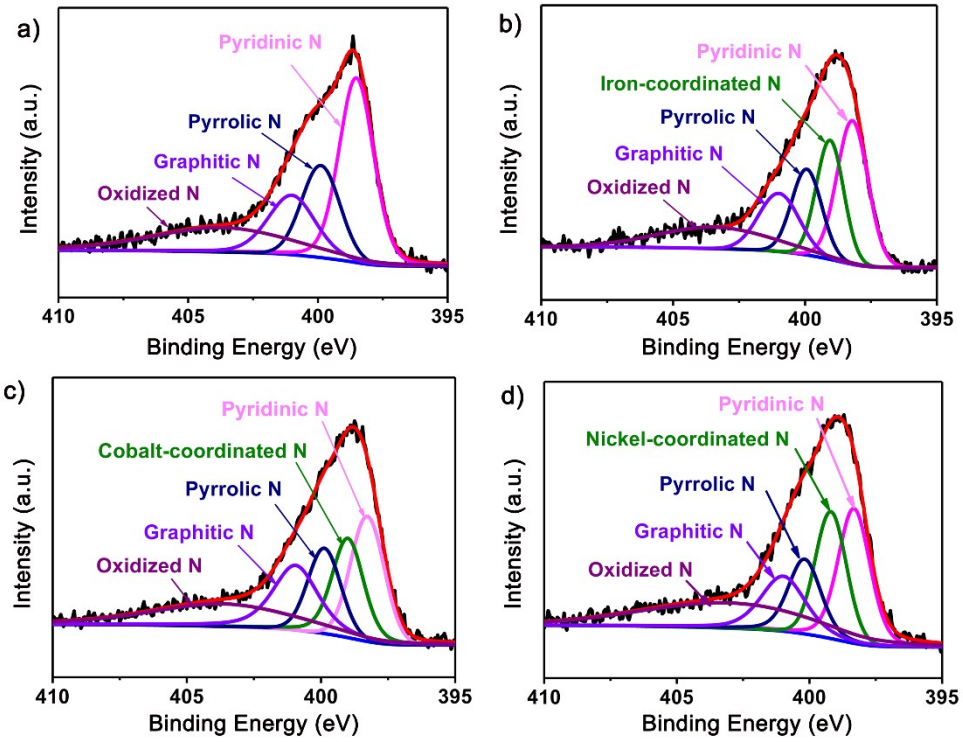

Figure S15. XPS N 1s spectra of a) N/BP, b) Fe-N/BP, c) Co-N/BP and d) Ni-N/BP.

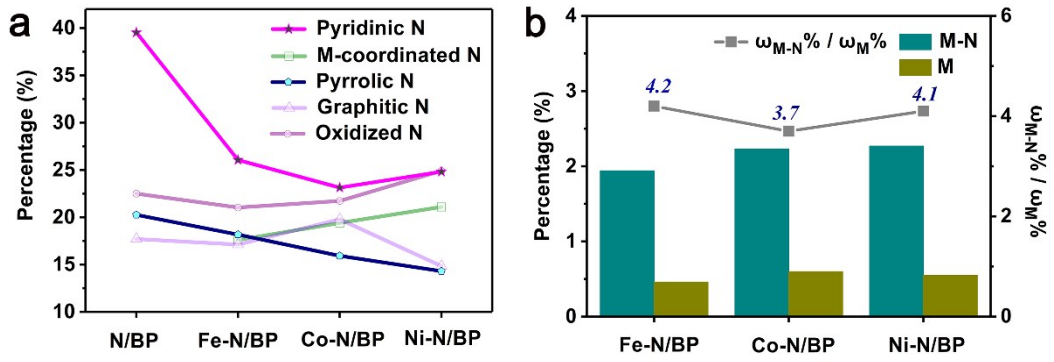

Figure S16. a) Relative content of various N species in the catalysts of N/BP, Fe-N/BP, Co-N/BP and Ni-N/BP. b)The metal-nitrogen percentage ($\omega_{M\text{-}N}\%$), metal percentage ($\omega_M\%$) and their ratios ($\omega_{M\text{-}N}\%/\omega_M\%$) of Fe-N/BP, Co-N/BP and Ni-N/BP.

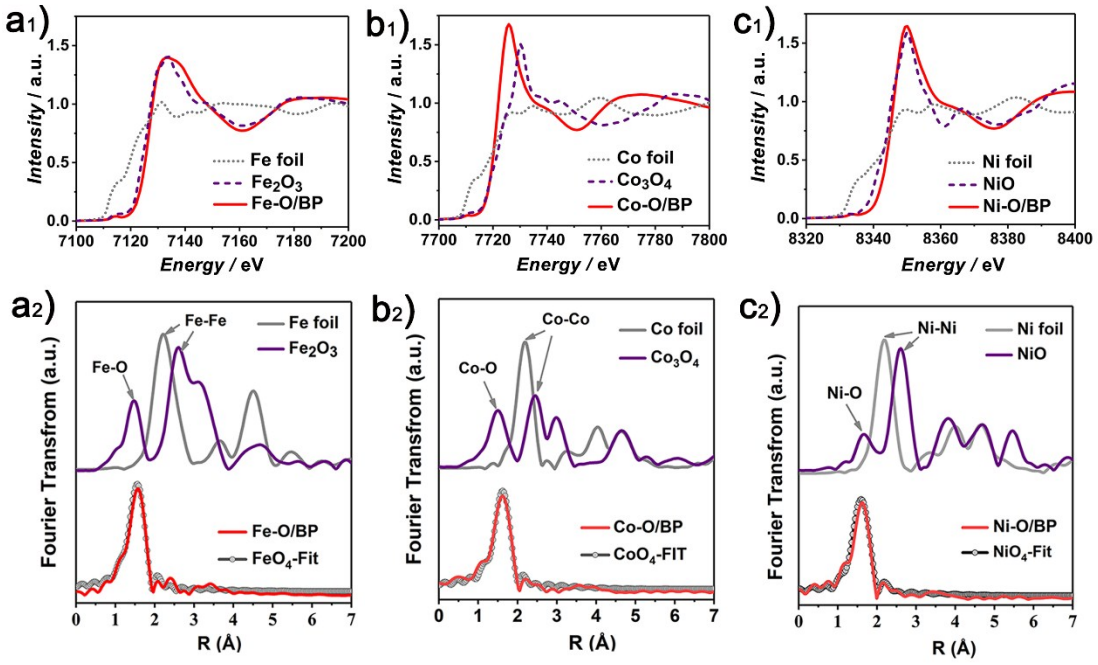

Figure S17. (a_1-c_1) Normalized XANES spectra at FM (Fe, Co, Ni) K-edge and (a_2-c_2) FT-EXAFS spectra of indicated samples and the R-space fitting for Fe-O/BP, Co-O/BP and Ni-O/BP. The fitting results in (a_2-c_2) show the FM atom is possibly coordinated by four oxygen atoms.

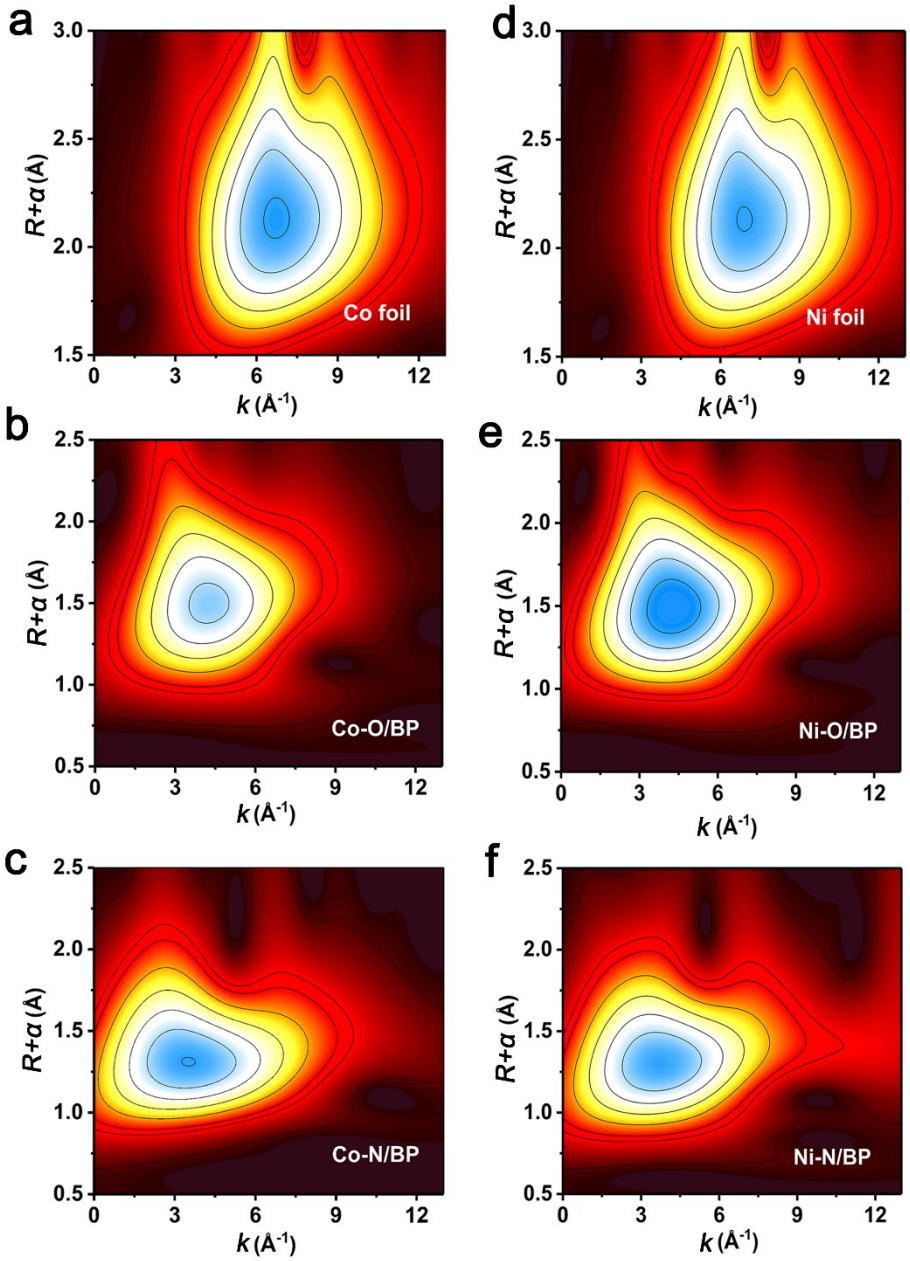

Figure S18. Wavelet transforms for the Co k^3-weighted EXAFS signals of (a) Co foil, (b) Co-O/BP, (c) Co-N/BP and Ni k^3-weighted EXAFS signals of (d) Ni foil, (e) Ni-O/BP, (f) Ni-N/BP with optimum resolutions at 2.0 Å.

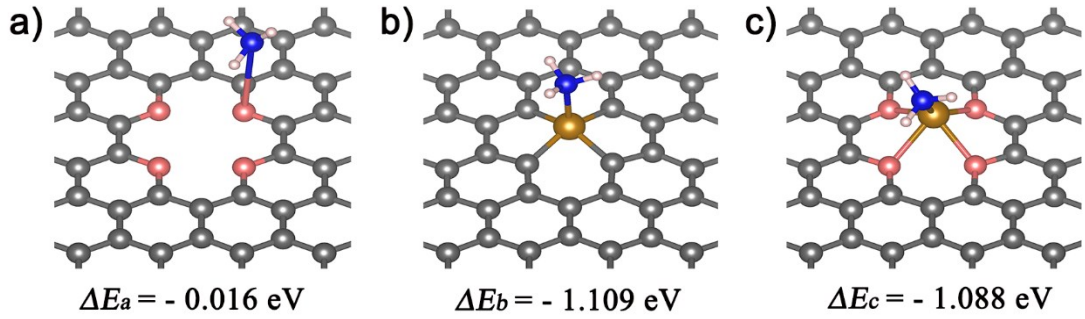

Figure S19. Geometric structures of a) O/BP, b) Fe/BP and c) Fe-O/BP with adsorption of NH_3. The gray, pink, brown, blue and white represent C, O, Fe, N and H atoms, respectively.

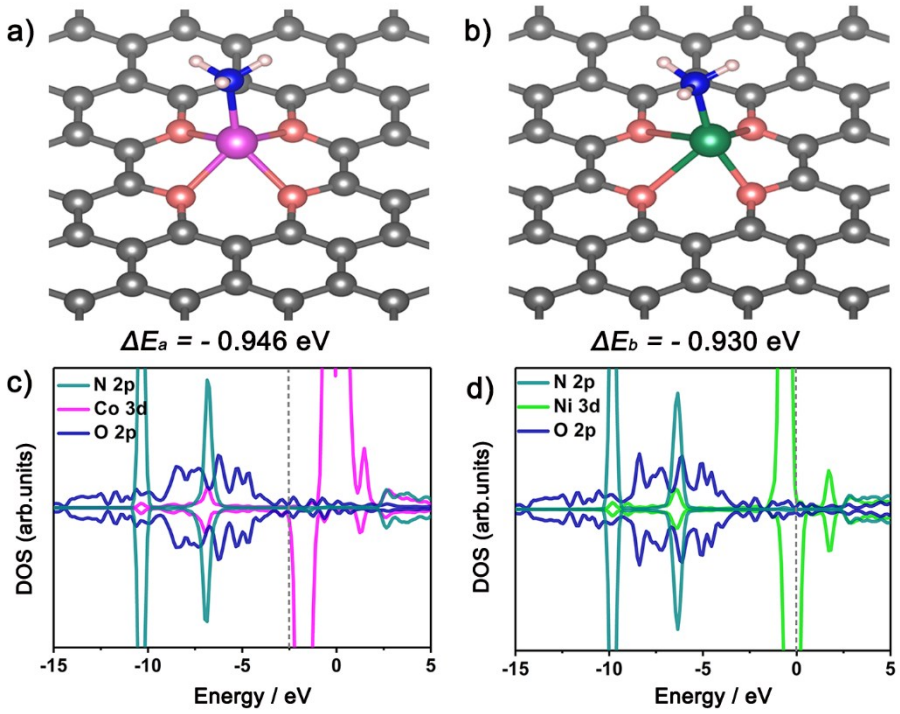

Figure S20. Geometric structures of (a) Co-O/BP and (b) Ni-O/BP with adsorption of NH_3. Density of states of (c) Co-O/BP and (d) Ni-O/BP with adsorption of NH_3. The gray, pink, magenta, green, blue and white represent C, O, Co, Ni, N and H atoms, respectively.

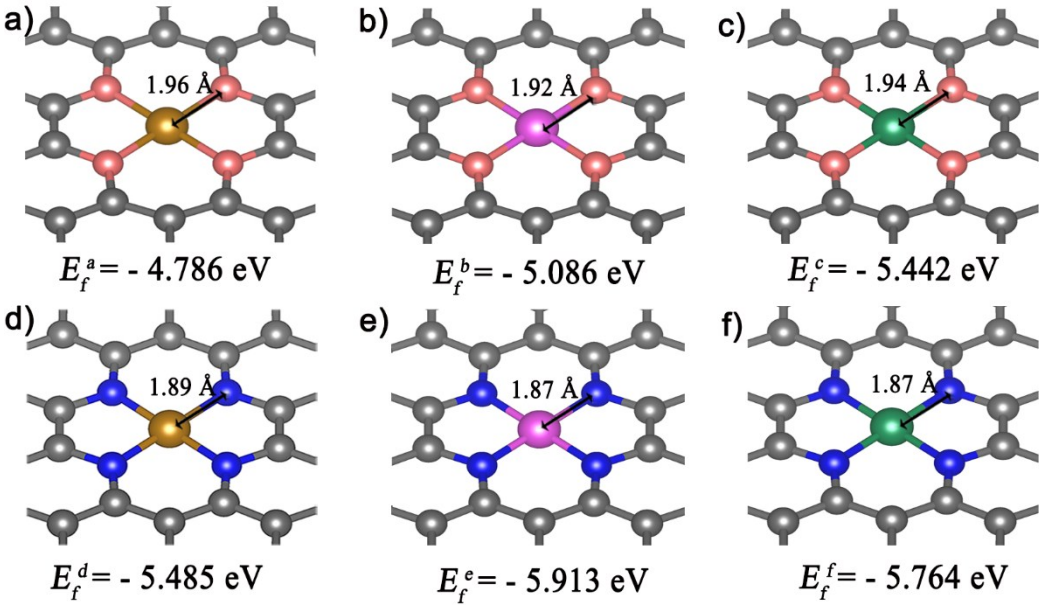

Figure S21. The configurations, formation energies, FM-O/FM-N bond lengths of (a) Fe-O/BP, (b) Co-O/BP, (c) Ni-O/BP, (d) Fe-N/BP, (e) Co-N/BP and (f) Ni-N/BP. The gray, pink, blue, brown, magenta and green represent C, O, N, Fe, Co and Ni atoms, respectively.

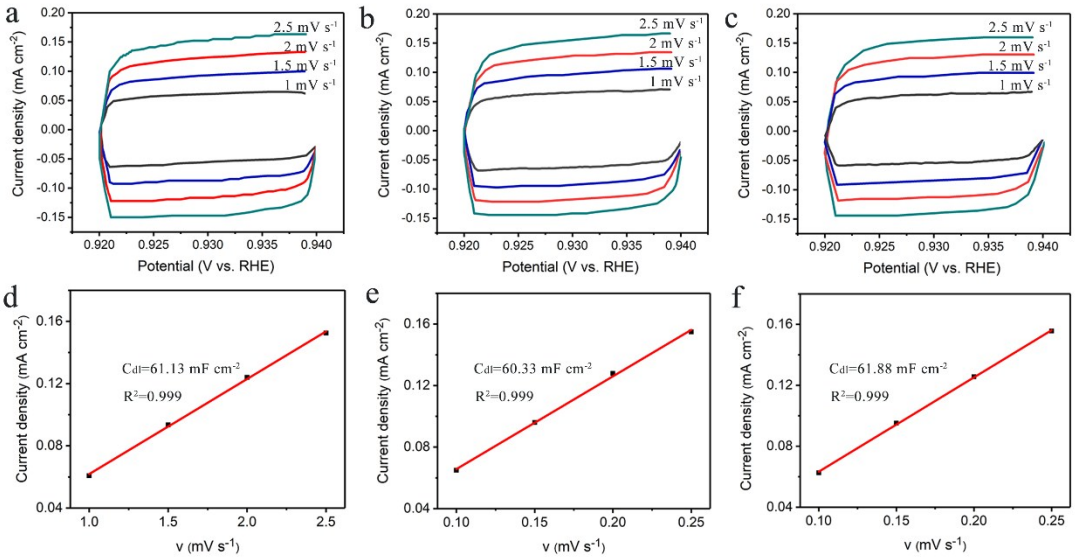

Figure S22. The ECSA estimation. (a) Cyclic voltammetry data of Fe-N/BP, Co-N/BP and Ni-N/BP at various scan rates. (b) Plots of current densities (taken at 0.930 V *vs.* RHE) as a function of scan rates. All the CV curves were obtained in nitrogen-saturated 0.5 M H_2SO_4.

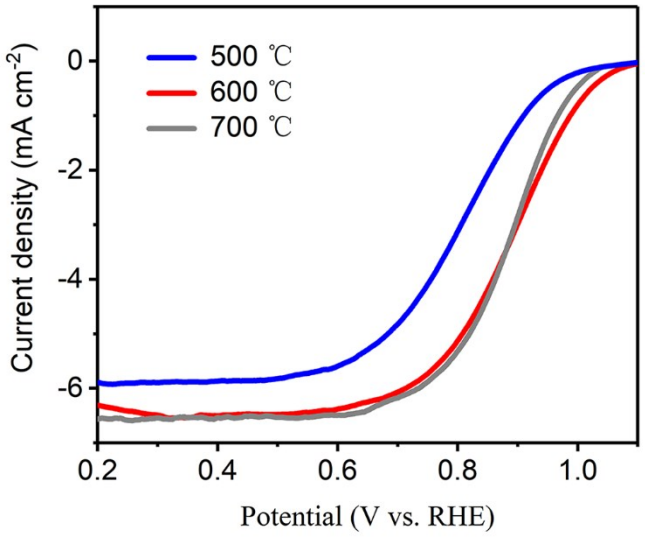

Figure S23. LSV curves of Fe-N/BP catalysts in O_2-saturated 0.1 M KOH. The catalysts was treated at the indicated heat-treatment temperatures.

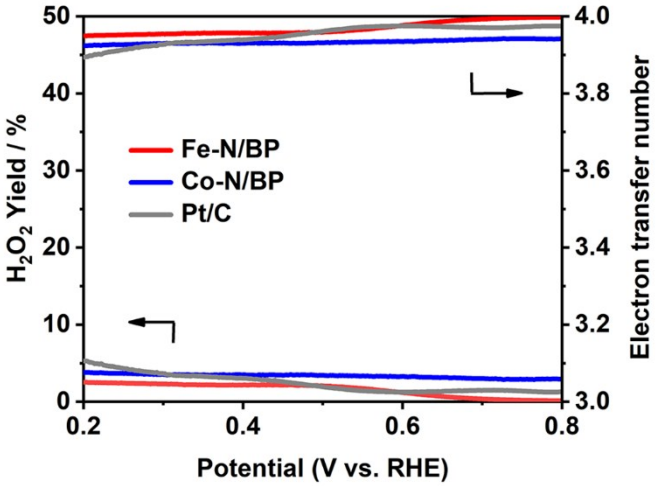

Figure S24. The electron transfer numbers and H_2O_2 yields of Fe-N/BP, Co-N/BP and Pt/C in 0.1 M KOH electrolytes.

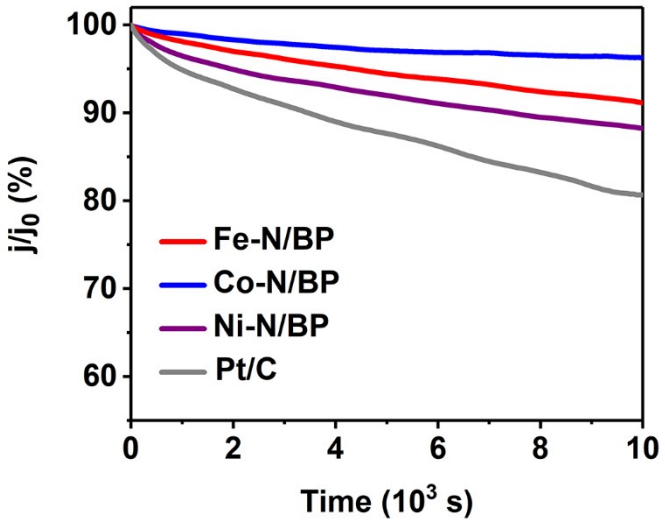

Figure S25. The stability evaluation of indicated catalysts by chronoamperometry at 0.5 V in O_2 saturated 0.1 M KOH solution at 1600 rpm.

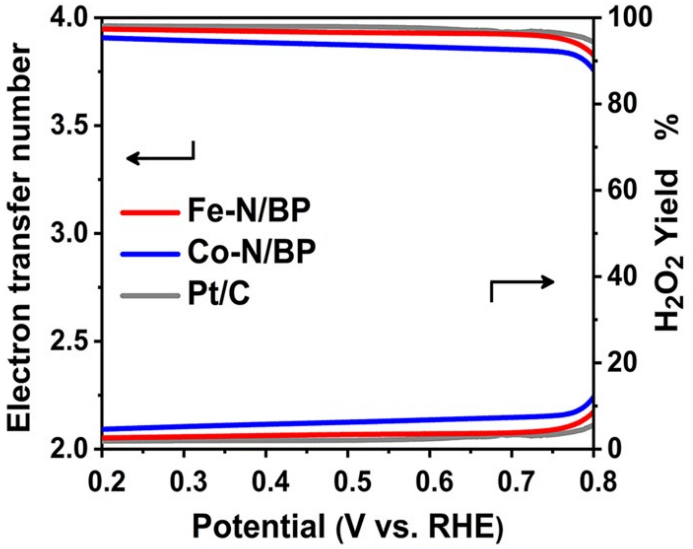

Figure S26. The electron transfer numbers and H_2O_2 yields of Fe-N/BP, Co-N/BP in 0.5 M H_2SO_4 and Pt/C in 0.1 M $HClO_4$ electrolytes.

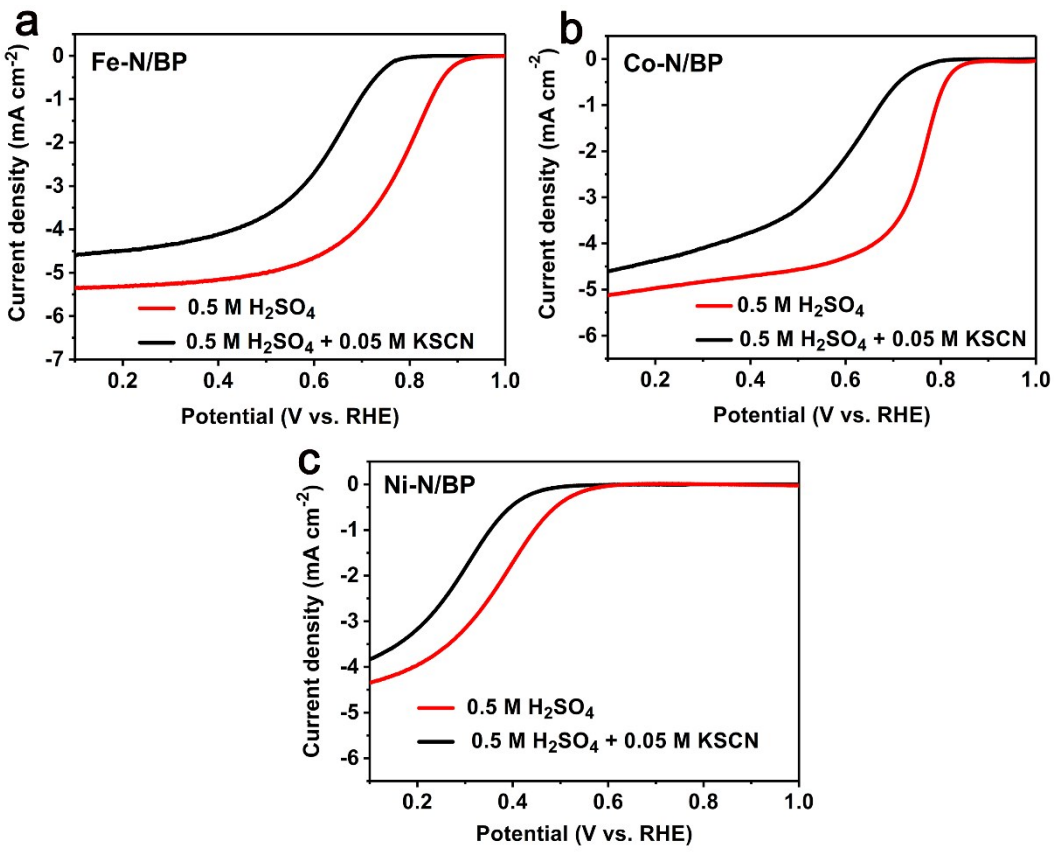

Figure S27. LSV curves of a) Fe-N/BP, b) Co-N/BP, c) Ni-N/BP before and after addition of 0.05 M KSCN in 0.5 M H_2SO_4.

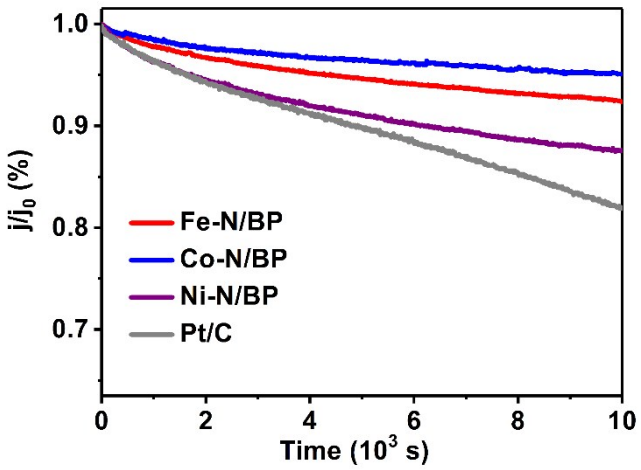

Figure S28. The stability evaluation of indicated catalysts by chronoamperometry at 0.5 V for 10,000 s. Test conditions: O_2-saturated 0.5 M H_2SO_4 (0.1 M $HClO_4$ for Pt/C), 1600 rpm.

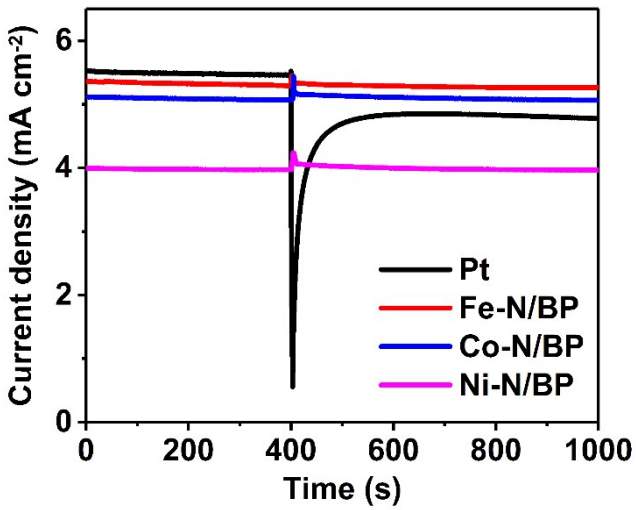

Figure S29. The methanol tolerance evaluation by chronoamperometry at 0.5 V in O_2 saturated 0.5 M H_2SO_4 (0.1 M $HClO_4$ for Pt/C) at 1600 rpm (injecting 1M methanol at 400 s).

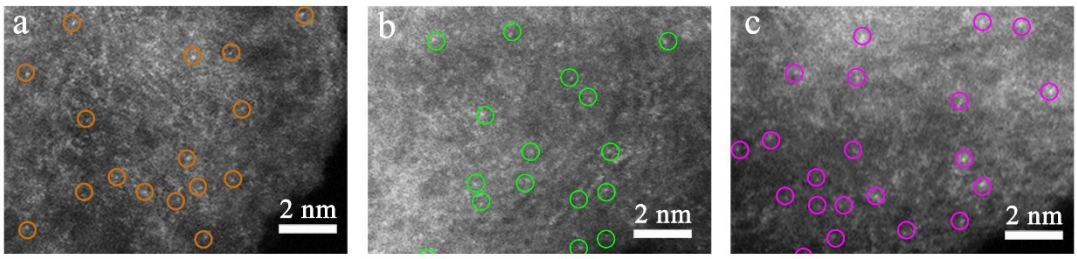

Figure S30. HAADF-STEM images of (a) Fe-N/BP, (b) Co-N/BP and (c) Ni-N/BP after the durability tests, showing the well maintained atomically dispersed FM atoms on BP2000 support as highlighted by color circles.

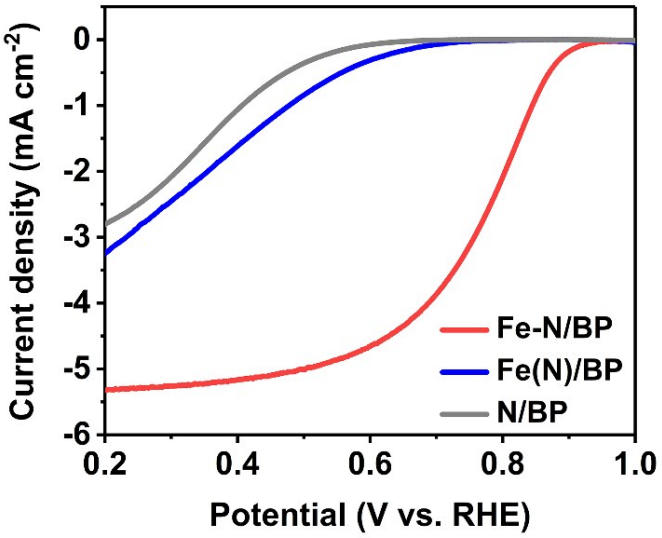

Figure S31. LSV curves of N/BP, Fe(N)/BP and Fe-N/BP in 0.5 M H_2SO_4.

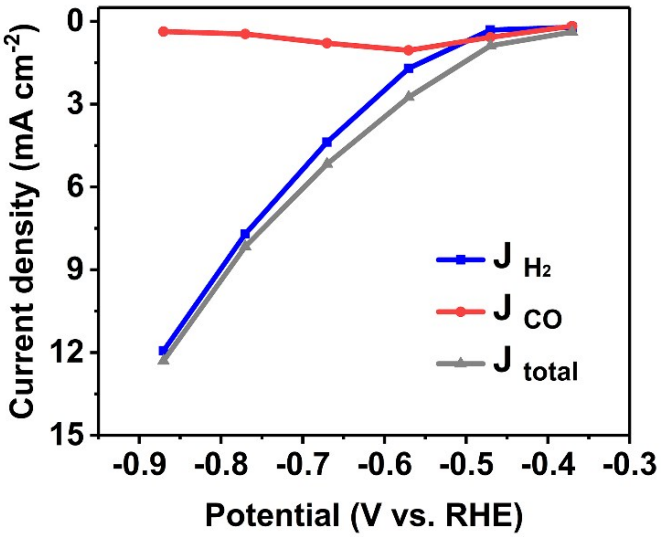

Figure S32. H_2, CO and total steady-state current densities of Fe-N/BP in CO_2-saturated 0.5 M $KHCO_3$. The catalyst mass loading is 0.2 mg cm^{-2}.

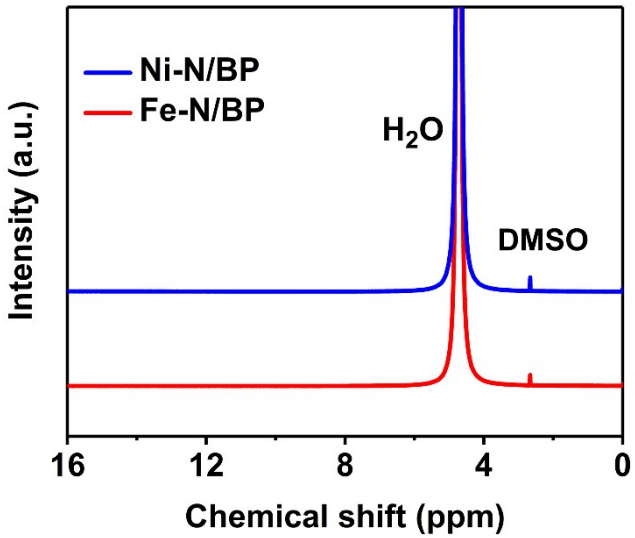

Figure S33. Representative NMR spectra of the electrolyte after CO_2 reduction electrolysis 3h at -0.9 V versus RHE for the Ni-N/BP and Fe-N/BP.

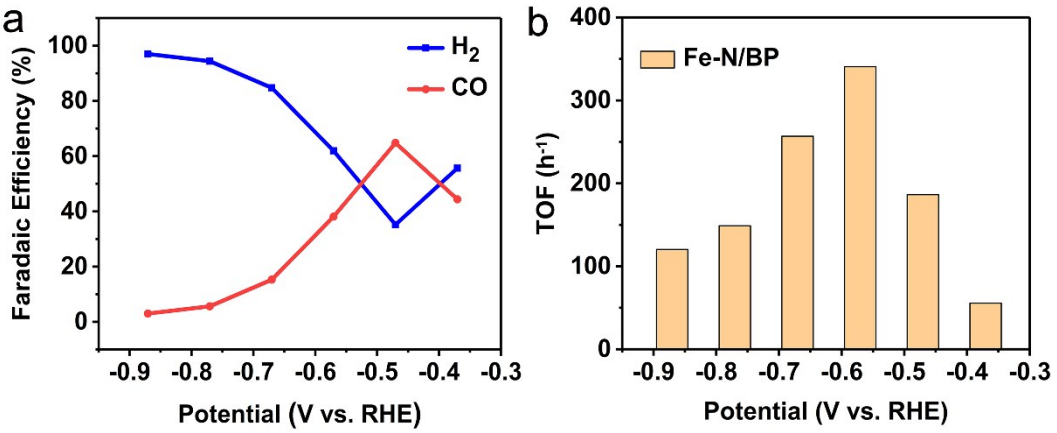

Figure S34. (a) Faradaic efficiencies of H_2 and CO and (b) TOF of Fe-N/BP in an H-cell test. The catalyst mass loading is 0.2 mg cm^{-2}.

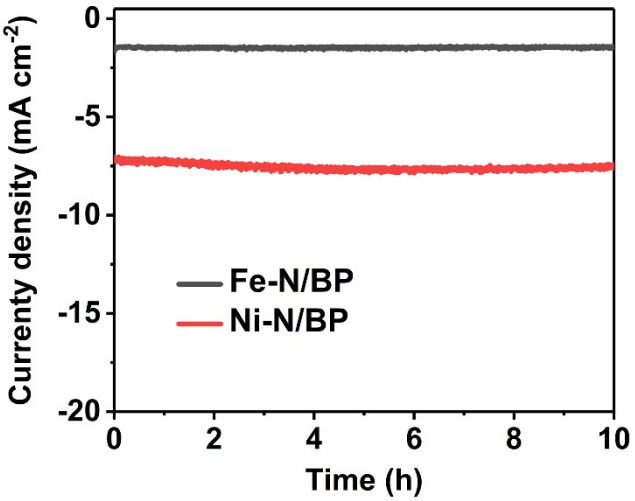

Figure S35. Chrono-Amperometry results for Fe-N/BP and Ni-N/BP at the potentials of -0.47 V vs. RHE and -0.73 vs. RHE, respectively. The catalyst mass loading is 0.5 mg cm^{-2}.

Table S1. Specific surface areas and pore size distributions of as-prepared materials.

Catalysts	Specific surface area / $m^2 g^{-1}$	Micropore area / $m^2 g^{-1}$	Micropore volume / $cm^3 g^{-1}$	External surface area / $m^2 g^{-1}$
BP	1215	876	0.39	330
Fe-N/BP	938	605	0.28	278

Table S2. Single-atom metal loadings of the FM-N/BP and some previously reported carbon supported SACs synthesized by the high temperature pyrolysis.

Sample	Metal loading	Measurement method	T (℃)	Reference
Ni-NCB	0.27 wt%	ICP	800	1
Pt_1-N/BP	0.4 wt%	ICP	750	2
ZnN_x/BP	0.3 wt%	ICP	900	3
Fe/NG-750	~0.6 wt%	ICP	750	4
$Pt_{1.1}/BP_{defect}$	1.1 wt%	ICP	900	5
Co-N/CNT	~ 0.1 at%	XPS	900	6
Ni-SAC@graphene oxide	0.44 at%	XPS	900	7
Fe-SACs	1.85 wt%	ICP	600	8
Fe-N/BP	1.6 wt% / 0.41 at%	ICP/XPS	600	**This work**
Co-N/BP	2.1 wt% / 0.6 at%	ICP/XPS	600	
Ni-N/BP	2.0 wt% / 0.55 at%	ICP/XPS	600	

Table S3. Surface elemental compositions of O/BP, N/BP and FM-N/BP determined by XPS.

Sample	C atom%	O atom%	N atom%	M atom%
O/BP	83.57	16.43	-	-
N/BP	91.27	2.54	6.19	-
Fe-N/BP	86.11	2.30	11.04	0.41
Co-N/BP	85.20	2.67	11.52	0.60
Ni-N/BP	86.37	2.29	10.79	0.55

Table S4. The contents of N in different chemical states for N/BP and FM-N/BP catalysts obtained from N 1s XPS results.

Sample	Pyridinic N %	M-coordinated N %	Pyrrolic N %	Graphitic N %	Oxidized N %
N/BP	39.52	-	20.26	17.71	22.51
Fe-N/BP	32.73	18.92	14.74	16.15	17.46
Co-N/BP	23.14	19.41	15.93	19.79	21.73
Ni-N/BP	29.07	23.79	20.06	17.01	10.05

Table S5. Fitting results of EXAFS for FM-O/BP by the IFEFFIT code.

Sample	path	*N*	*R* (Å)	σ^2(*10^{-3} Å^2)	ΔE_0 (eV)	*R* factor (%)
Fe-O/BP	Fe-O	3.8	2.00	1.09	0.76	0.11
Co-O/BP	Co-O	3.8	1.93	0.59	4.43	0.06
Ni-O/BP	Ni-O	4.2	1.98	0.58	2.66	0.06

N : coordination numbers; *R* : bond distance; σ^2 : Debye-Waller factors; ΔE_0: the inner potential correction; *R* factor: goodness of fit. Error bounds (accuracies) that characterize the structural parameters obtained by EXAFS spectroscopy were estimated as $N \pm 20\%$; $R \pm 1\%$; $\sigma^2 \pm 20\%$; $\Delta E_0 \pm 20\%$. $S_0^2 = 0.98$ was fixed to all the samples.

Table S6. Fitting results of EXAFS for FM-N/BP by the IFEFFIT code.

Sample	path	*N*	*R* (Å)	σ^2(*10^{-3} Å^2)	ΔE_0 (eV)	*R* factor (%)
Fe-N/BP	Fe-N	4.1	2.03	2.80	1.12	0.60
Co-N/BP	Co-N	4.0	1.86	7.99	-7.52	0.18
Ni-N/BP	Ni-N	3.9	1.75	6.67	-8.98	0.14

N : coordination numbers; *R*: bond distance; σ^2 : Debye-Waller factors; ΔE_0: the inner potential correction; *R* factor: goodness of fit. Error bounds (accuracies) that characterize the structural parameters obtained by EXAFS spectroscopy were estimated as $N \pm 20\%$; $R \pm 1\%$; $\sigma^2 \pm 20\%$; $\Delta E_0 \pm 20\%$. S_0^2 was fixed to 0.98 as determined from Fe foil (Co foil or Ni foil) fitting.

Table S7. Comparison of ORR activities of various Fe-N-C catalysts in the alkaline medium.

Sample	Electrolytes	$E_{1/2}$ (V)	Reference
Fe-N-SCCFs	0.1 M KOH	0.883	9
3D MPC	0.1 M KOH	0.88	10
FeP_x/Fe–N–C/NPC	0.1 M KOH	0.86	11
FeN_2/NOMC-3	0.1 M KOH	0.863	12
CAN-Pc(Fe)	0.1 M KOH	0.74	13
Fe-NPC	0.1 M KOH	0.885	14
Fe-N-C HNSs	0.1 M KOH	0.87	15
Fe_{SA}-N-C	0.1 M KOH	0.891	16
Fe-N-C-900	0.1 M KOH	0.89	17
Fe-N/BP	0.1 M KOH	0.90	**This work**

Table S8. Comparison of ORR activities of various Fe-N-C catalysts in acid media.

Sample	Electrolytes	$E_{1/2}$ (V)	Reference
Fe-N/CNT-2	0.1 M $HClO_4$	0.77	18
Fe_1-N-C	0.5 M H_2SO_4	0.715	
Fe_2-N-C	0.5 M H_2SO_4	0.78	19
Fe_3-N-C	0.5 M H_2SO_4	0.762	
Fe-N-C-950	0.1 M $HClO_4$	0.78	20
Fe_{SA}-N-C	0.1 M $HClO_4$	0.776	16
Fe-NC SAC	0.1 M $HClO_4$	0.68	21
Fe-N-DSC	0.5 M H_2SO_4	0.65	22
C-AFC©ZIF-8	0.1 M $HClO_4$	0.75	23
(CM+PANI)-Fe-C	0.5 M H_2SO_4	0.80	24
p-Fe–NCNF	0.1 M $HClO_4$	0.74	25
Fe-N/BP	0.5 M H_2SO_4	0.78	**This work**

Table S9. Performance comparison for electrocatalytic CO_2 reduction to CO in $KHCO_3$ for Ni-N-C catalysts.

Sample	Electrolytes ($KHCO_3$)	Onset potential (V vs. RHE)	Highest faradaic efficiency (%)	Reference
Ni-NC SACs	0.5 M	~ -0.2	89	21
Ni-N-C	0.1 M	~ -0.42	85	26
Ni-N-C	0.1 M	~ -0.6	90	7
Ni-NCB	0.5 M	-0.41	~99	1
Ni SAs/N-C	0.5 M	~ -0.5	72	27
Ni-N/BP	0.5 M	-0.42	88	**This work**

Reference

1. T. Zheng; K. Jiang; N. Ta; Y. Hu; J. Zeng; J. Liu; H. Wang, *Joule* 2019, **3,** 265-278.

2. J. Liu; M. Jiao; L. Lu; H. M. Barkholtz; Y. Li; Y. Wang; L. Jiang; Z. Wu; D. J. Liu; L. Zhuang; C. Ma; J. Zeng; B. Zhang; D. Su; P. Song; W. Xing; W. Xu; Y. Wang; Z. Jiang; G. Sun, *Nat. Commun.* 2017, **8,** 15938.

3. P. Song; M. Luo; X. Liu; W. Xing; W. Xu; Z. Jiang; L. Gu, *Adv. Funct. Mater.* 2017, **27,** 1700802.

4. C. Zhang; S. Yang; J. Wu; M. Liu; S. Yazdi; M. Ren; J. Sha; J. Zhong; K. Nie; A.-S. Jalilov; Z. Li; H. Li; B.-I. Yakobson; Q. Wu; E. Ringe; H. Xu; P.-M. Ajayan; J.-M. Tour, *Adv. Energy Mater.* 2018, **8,** 1703487.

5. J. Liu; M. Jiao; B. Mei; Y. Tong; Y. Li; M. Ruan; P. Song; G. Sun; L. Jiang; Y. Wang; Z. Jiang; L. Gu; Z. Zhou; W. Xu, *Angew. Chem. Int. Ed.* 2019, **58,** 1163-1167.

6. Y. Liu; F. Chen; W. Ye; M. Zeng; N. Han; F. Zhao; X. Wang; Y. Li, *Adv. Funct. Mater.* 2017, **27,** 1606034.

7. T. Möller; W. Ju; A. Bagger; X. Wang; F. Luo; T. Ngo Thanh; A. S. Varela; J. Rossmeisl; P. Strasser, *Energ. Environ. Sci.* 2019, **12,** 640-647.

8. H. Yang; L. Shang; Q. Zhang; R. Shi; G. I. N. Waterhouse; L. Gu; T. Zhang, *Nat. Commun.* 2019, **10,** 4585.

9. B. Wang; X. Wang; J. Zou; Y. Yan; S. Xie; G. Hu; Y. Li; A. Dong, *Nano Lett.* 2017, **17,** 2003-2009.

10. W. Wang; W. Chen; P. Miao; J. Luo; Z. Wei; S. Chen, *ACS Catal.* 2017, **7,** 6144-6149.

11. Q. Qin; H. Jang; P. Li; B. Yuan; X. Liu; J. Cho, *Adv. Energy Mater.* 2019, **9,** 1803312.

12. H. Shen; E. Gracia-Espino; J. Ma; H. Tang; X. Mamat; T. Wagberg; G. Hu; S. Guo, *Nano Energy* 2017, **35,** 9-16.

13. S. Yang; Y. Yu; M. Dou; Z. Zhang; L. Dai; F. Wang, *Angew. Chem. Int. Ed.* 2019, **58,** 14724-14730.

14. Y. Li; B. Chen; X. Duan; S. Chen; D. Liu; K. Zang; R. Si; F. Lou; X. Wang; M. Rønning; L. Song; J. Luo; D. Chen, *Appl. Catal. B: Environ.* 2019, **249,** 306-315.

15. Y. Chen; Z. Li; Y. Zhu; D. Sun; X. Liu; L. Xu; Y. Tang, *Adv. Mater.* 2019, **31,** e1806312.

16. L. Jiao; G. Wan; R. Zhang; H. Zhou; S. H. Yu; H. L. Jiang, *Angew. Chem. Int. Ed.* 2018, **57,** 8525-8529.

17. C. Zhu; Q. Shi; B. Z. Xu; S. Fu; G. Wan; C. Yang; S. Yao; J. Song; H. Zhou; D. Du; S. P. Beckman; D. Su; Y. Lin, *Adv. Energy Mater.* 2018, **8,** 1801956.

18. D. Xia; X. Yang; L. Xie; Y. Wei; W. Jiang; M. Dou; X. Li; J. Li; L. Gan; F. Kang, *Adv. Funct. Mater.* 2019, **29,** 1906174.

19. W. Ye; S. Chen; Y. Lin; L. Yang; S. Chen; X. Zheng; Z. Qi; C. Wang; R. Long; M. Chen; J. Zhu; P. Gao; L. Song; J. Jiang; Y. Xiong, *Chem* 2019, **5,** 2865-2878.

20. M. Xiao; J. Zhu; L. Ma; Z. Jin; J. Ge; X. Deng; Y. Hou; Q. He; J. Li; Q. Jia; S. Mukerjee; R. Yang; Z. Jiang; D. Su; C. Liu; W. Xing, *ACS Catal.* 2018, **8,** 2824-2832.

21. L. Zhao; Y. Zhang; L.-B. Huang; X.-Z. Liu; Q.-H. Zhang; C. He; Z.-Y. Wu; L.-J. Zhang; J. Wu; W. Yang; L. Gu; J.-S. Hu; L.-J. Wan, *Nat. Commun.* 2019, **10,** 1278.

22. Z. Huang; H. Pan; W. Yang; H. Zhou; N. Gao; C. Fu; S. Li; H. Li; Y. Kuang, *ACS Nano* 2018, **12,** 208-216.

23. Y. Ye; F. Cai; H. Li; H. Wu; G. Wang; Y. Li; S. Miao; S. Xie; R. Si; J. Wang; X. Bao, *Nano Energy* 2017, **38,** 281-289.

24. H.-T. Chung; D.-A. Cullen; D. Higgins; B.-T. Sneed; E.-F. Holby; K.-L. More; P. Zelenay, *Science* 2017, **357,** 479-484.

25. B.-C. Hu; Z.-Y. Wu; S.-Q. Chu; H.-W. Zhu; H.-W. Liang; J. Zhang; S.-H. Yu, *Energ. Environ. Sci.* 2018, **11,** 2208-2215.

26. W. Ju; A. Bagger; G.-P. Hao; A.-S. Varela; I. Sinev; V. Bon; B. Roldan-Cuenya; S. Kaskel; J. Rossmeisl; P. Strasser, *Nat. Commun.* 2017, **8,** 944.

27. C. Zhao; X. Dai; T. Yao; W. Chen; X. Wang; J. Wang; J. Yang; S. Wei; Y. Wu; Y. Li, *J. Am. Chem. Soc.* 2017, **139,** 8078-8081.